Communication

Numerical Simulation of Fluid Flow in a Gas-Stirred Ladle Using a Particle-Free Surface Coupled Model

BOHONG ZHU, BO ZHANG, and KINNOR CHATTOPADHYAY

A particle-free surface coupled (PFC) model was developed using the Eulerian–Eulerian approach to predict fluid flow behavior in a gas-stirred ladle. The relative parameters of the model have been optimized, and the model was validated against measured values. The present model can simultaneously predict the bubble trajectories, free surface fluctuations, and the formation of slag open-eye in a wide range of gas flow rates.

https://doi.org/10.1007/s11663-020-01824-w

Gas-stirred ladles play an essential role in performing various metallurgical operations during the secondary refining process. The injected gas through the ladle bottom helps to promote stirring of melt and promotes chemical reactions, enhances inclusion removal, and helps to homogenize the temperature and chemistry of the liquid steel. The most intensive heat and mass transfer occur in the bubbly plume region, and hence, it is of paramount importance to have a deep understanding of the fluid flow behavior in this region.[1–3]

Currently, numerical simulation is considered as an effective tool to investigate this topic; there are limitations in performing trials at high temperature and visualization at high temperature is almost impossible. Based on the Eulerian–Lagrangian approach, the discrete phase model (DPM) and volume of fluid (VOF) coupled model has become the preferred method to model the gas-stirred ladle system. Cloete *et al.*[4] used the DPM-VOF model for investigating the influence of a large number of operating and design variables on the fluid flow and mixing time in the ladle. Liu *et al.*[5] applied the DPM-VOF model to predict the bubble trajectories and interfacial behavior of slag/metal in a gas-stirred ladle. Li *et al.*[6–8] added the large eddy simulation model to the DPM-VOF model for investigating the effects of multiscale eddies on fluid flow and studying the unsteady state of the open-eye. Significantly, the limitations of the Eulerian–Lagrangian approach are pretty well known today. First, the application of this approach assumes that the particle volume is strictly limited to 10 to 12 pct and the impact among particles is ignored.[9] Second, the discrete phase does not occupy any space continuous volume; thus, the effect of the volume fraction of the discrete phase on the continuous phase is ignored. To address this problem, Sheng and Irons[10] introduced a method of calculating the time-averaged bubble volume fraction using the statistics of the number and residence time of bubbles in the given cells:

$$\alpha_g = \frac{1}{TV_{\text{cell}}} \sum_{n=1}^{N} V_{\text{bub},n} dt_n, \qquad [1]$$

where V_{cell} is the grid cell volume; N is the number of bubble particles released from the gas inlet; and $V_{\text{bub},n}$ and dt_n are the volume and residence time of the nth bubble in the control cell volume, respectively. However, Low and Zhu[11] reported that the result predicted by the Eulerian–Lagrangian approach has a large error under a higher gas flow rate, the time-averaged gas volume fraction is still affected by cell size and the released particle number, and the particle stochastic trajectory also increases the instability of spatial distribution of the gas volume fraction.

However, for the Eulerian–Eulerian approach, the phases are treated as interpenetrating fluids and the laws of conservation of mass and momentum are satisfied by each phase individually. Accordingly, the aforementioned problem does not arise with the Eulerian–Eulerian approach. In view of this, the VOF model has been employed in the ladle simulation. Because of the ability of the VOF model to track the sharp interface, this model can be mainly used for predicting slag-steel interface behaviors such as slag entrainment[12,13] and formation of slag open-eye.[13,14] However, Cao and Nastac[15] recently compared the DPM-VOF model and VOF model and found that the VOF model can reflect the fluctuation of liquid-free surface, but it fails to accurately capture the bubble motion in the plume. This is because the bubble motion in molten steel is interpenetrating, while the VOF model prefers to model the interface motion. Moreover, the Eulerian model[2,11] also has been applied in the simulation of the gas-stirred ladle. Due to the effects of interactions between the gas phase and liquid phase can be fully considered, the Eulerian model exhibits outstanding ability to predict

BOHONG ZHU and BO ZHANG are with the College of Metallurgy and Materials Engineering, Hunan University of Technology, Zhuzhou 412007, China. Contact e-mail: metal.eng@hut.edu.cn KINNOR CHATTOPADHYAY is with the Department of Materials Science and Engineering, University of Toronto, Toronto, ON M5S 3E4, Canada.

Manuscript submitted October 25, 2019.
Article published online April 1, 2020.

the bubbly plume structure in a gas-stirred ladle. Unfortunately, the aforementioned Eulerian model was developed based on the assumption that the liquid-free surface is treated as flat, and hence, the effect of the fluctuation of the free surface on fluid flow was neglected. Significantly, there is the potential to integrate the advantages of the VOF model and the Eulerian model to develop a model for predicting the various fluid flow phenomena in the gas-stirred ladle.

In this study, two submodels, *i.e.*, the particle model and free surface model, are integrated for a coupled model—the particle-free surface coupled (PFC) model—under the Eulerian–Eulerian framework. The continuity and Navier–Stokes equations are used for calculating the transfers of momentum and mass between the different phases as follows:

$$\frac{\partial}{\partial t}(\alpha_i \rho_i) + \nabla \cdot (\alpha_i \rho_i \vec{v}_i) = 0 \quad [2]$$

$$\frac{\partial}{\partial t}(\alpha_i \rho_i \vec{v}_i) + \nabla \cdot (\alpha_i \rho_i \vec{v}_i \vec{v}_i) = -\alpha_i \nabla P + \alpha_i \rho_i \vec{g} + \nabla \cdot \left[\alpha_i (\mu_l + \mu_{l,t}) \left(\nabla \vec{v}_i + (\nabla \vec{v}_i)^T\right)\right] + \vec{F}_{ij} \quad [3]$$

where α_i, ρ_i, $\vec{v}_i$, P, and $\vec{g}$ are the volume fraction, density, phase-averaged velocity, pressure, and gravity acceleration. μ_l is the molecular viscosity of the liquid phase, and $\mu_{l,t}$ is the turbulent viscosity. $\vec{F}_{ij}$ presents the total interphase forces, including the surface tension force, drag force, and nondrag forces.

The gas bubble phase is considered as the dispersed phase, while the molten metal phase, slag phase, and top gas phase are treated as the continuous phase. The initial bubble diameter (d_g) at the inlet is calculated using Eq. [4] and obeys the ideal gas law during the rising process.[16,17]

$$d_g = 0.624 Q_g^{0.406} \quad [4]$$

The interactions between the dispersed phase and continuous phase are modeled using the Particle submodel *via* the interfacial area density (A_{cg}):

$$A_{cg} = \frac{6\alpha_g}{d_g} \quad [5]$$

$$\alpha_g = \begin{cases} \max(\alpha_g,\ 10^{-7}) & \text{if } (\alpha_g \le 0.8) \\ \max(4 \cdot (1-\alpha_g),\ 10^{-7}) & \text{if } (\alpha_g > 0.8) \end{cases} \quad [6]$$

For nondrag forces, the modified interfacial area density (A'_{cg}) is applied:

$$A'_{cg} = \left(\frac{1-\alpha_g}{1-\alpha'_g}\right)^5 A_{cg} \quad [7]$$

$$\alpha'_g = \begin{cases} \alpha_g & \text{if}(\alpha_g \le 0.25) \\ 0.393855 - 0.5142\alpha_g & \text{if}(0.25 < \alpha_g \le 0.6) \\ 0.05 & \text{if}(\alpha_g > 0.6) \end{cases} \quad [8]$$

Therefore, the total interphase force between the dispersed phase (g) and continuous phase (c), $\vec{F}_{cg}$, in Eq. [3] includes the drag force ($\vec{F}^D_{cg}$), lift force ($\vec{F}^L_{cg}$), virtual mass force ($\vec{F}^{VM}_{cg}$), and turbulent dispersion force ($\vec{F}^{TD}_{cg}$) as follows:

$$\vec{F}_{cg} = \vec{F}^D_{cg} + \vec{F}^L_{cg} + \vec{F}^{VM}_{cg} + \vec{F}^{TD}_{cg} \quad [9]$$

In addition, the interactions between the continuous phases (c or c') are modeled using the free surface model, and the interfacial area density ($A_{cc'}$) between the two phases can be expressed as

$$A_{cc'} = \frac{2|\nabla \alpha_c||\nabla \alpha_{c'}|}{|\nabla \alpha_c| + |\nabla \alpha_{c'}|} \quad [10]$$

The total interphase force between the continuous phases, $\vec{F}_{cc'}$, in Eq. [3] includes the drag force ($\vec{F}^D_{cg}$), and the surface tension force ($\vec{F}^{ST}_{cc'}$) can be expressed as

$$\vec{F}_{cc'} = \vec{F}^D_{cc'} + \vec{F}^{ST}_{cc'} \quad [11]$$

In a gas-stirred ladle, the bubbly plume structure is determined by the interactions between the liquid metal phase and the argon gas phase ($\vec{F}_{lg}$), as shown in Eq. [9]. To obtain the optimal coefficients of interphase forces, the Wood's metal ladle system is built on the basis of Xie *et al.*'s experiments.[18] The detailed model structure of Wood's metal ladle system can be seen in Figure 1(a).

The number of elements is created by ANSYS ICEM software (ANSYS, Inc., Canonsburg, PA, USA). A mesh sensitivity analysis for the PFC model has been conducted using three different meshes, which correspond with the number of control volume elements of 218,000, 350,000, and 485,000. It was found that the meshes with 350,000 and 485,000 elements produced quite similar simulation results. Thus, the mesh with 350,000 elements is suitable for the current studies, and the minimum quality metrics criterion of mesh is greater than 0.53. To obtain more detailed information in the regions of bubbly plume and free surface, a densely packed mesh is applied, as shown in Figure 2. It should be noticed that the top gas phase above the liquid-free surface is treated as the continuous phase, which is different from the injected gas phase. The injected gas phase can float up in the top gas phase due to the density difference and finally leave the calculation domain from the degassing condition boundary.[5] All numerical calculations have been finished using the ANSYS CFX-2019R1 software, and the differential equations

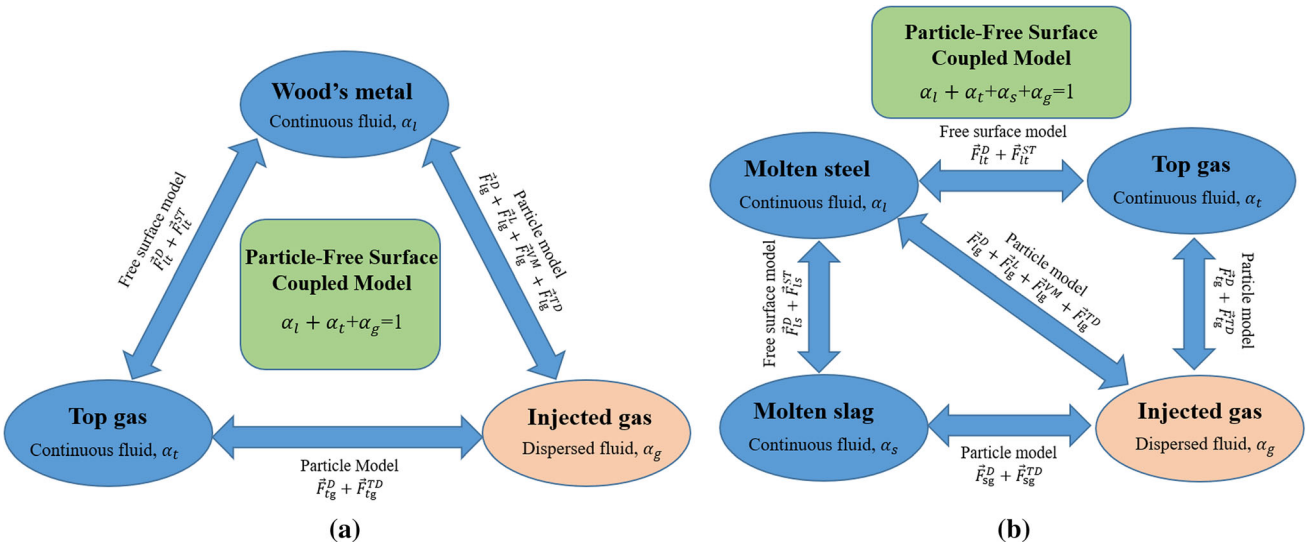

Fig. 1—Model structure and interaction between phases: (*a*) Wood's metal ladle system and (*b*) industrial scale ladle system.

Table I. Dimensional Parameters and Material Properties

Wood's metal ladle[18]			
Diameter of Wood's metal vessel, m	0.4	viscosity of Wood's metal, Pa·s	0.0042
Bath height of Wood's metal, m	0.37	surface tension of Wood's metal, N/m	0.46
Diameter of gas inlet, m	0.003	temperature of Wood's metal, K	373
Density of Wood's metal, kg/m^3	9400	density of nitrogen gas (STP), kg/m^3	1.25
Industrial ladle system			
Upper diameter of ladle, m	3.25	viscosity of molten steel, Pa·s	0.006
Bottom diameter of ladle, m	2.91	viscosity of slag, Pa·s	0.06
Bath height of molten steel, m	2.65	viscosity of argon gas, Pa·s	2.12×10^{-5}
Diameter of gas inlet, m	0.14	surface tension of metal/gas, N/m	1.5
Initial thickness of slag, m	0.1	surface tension of slag/gas, N/m	0.58
Density of molten steel, kg/m^3	7020	surface tension of metal/slag, N/m	1.15
Density of slag, kg/m^3	3500	temperature of molten steel, K	1873
Density of Argon gas, kg/m^3	1.623	gas flow rate, L/min	150 to 600

were solved by iteration until the value of the root-mean-square normalized residual taken across the entire domain for variables was less than 1×10^{-5}. Other model parameters can be seen in Table I.

Figure 3 shows the effects of the different interphase forces on the bubbly plume structure. For the drag force, its magnitude is directly influenced by the drag coefficient. Table II presents six correlations for the drag coefficient model, which are commonly adopted in gas-stirred systems. Figure 3(a) shows the results of models A and E, which agree well with the measured results, but the results predicted by models B through D are greatly overestimated. At the region of the bubbly plume, $x = -0.05$ to 0.05 m, models A and E take the value of 0.44 to 0.47 and the drag coefficients of models B through D are about 2.54 to 2.66. This is due to the shapes of the gas bubbles, such as sphere, ellipse, and cap, being treated as a factor in the drag coefficients of models B through D. In this study, the initial bubble diameter calculated using Eq. [4] is nearly 19 mm and bubbles of this size are no longer spherical in the actual process. It should be noticed that the drag coefficients of bubbles, which have the same diameter but different shapes, are extremely different. However, in the particle submodel, the interfacial area is calculated based on the assumption that the bubble is a spherical shape, resulting in the overestimation of models B, C, and E. Therefore, the drag coefficient model, Schiller and Naumann[19] or Morsi and Alexander,[23] is chosen in the present PFC model.

Some researchers[11,24] insisted that the virtual mass force is negligible, because the gas bubble velocity gradient is very small in the actual process. However, this force also has been considered in some reduced scale models,[6–8,15] due to the bubble velocity gradient becoming larger after the treatments of the similarity principle. Duan *et al.*[17] modeled the reduced scale model and found that the virtual mass force has a significant impact on the distribution of the gas volume fraction even if its effect on the vertical liquid velocity is minor. Figure 3(b) presents the effect of the virtual mass coefficient on the distribution of the gas volume fraction. The height of the bubbly plume increases as the virtual mass coefficient increases from 0 to 0.07, but it decreases as the virtual mass coefficient increases from 0.1 to 0.5. For the bottom stirring condition, the virtual mass force

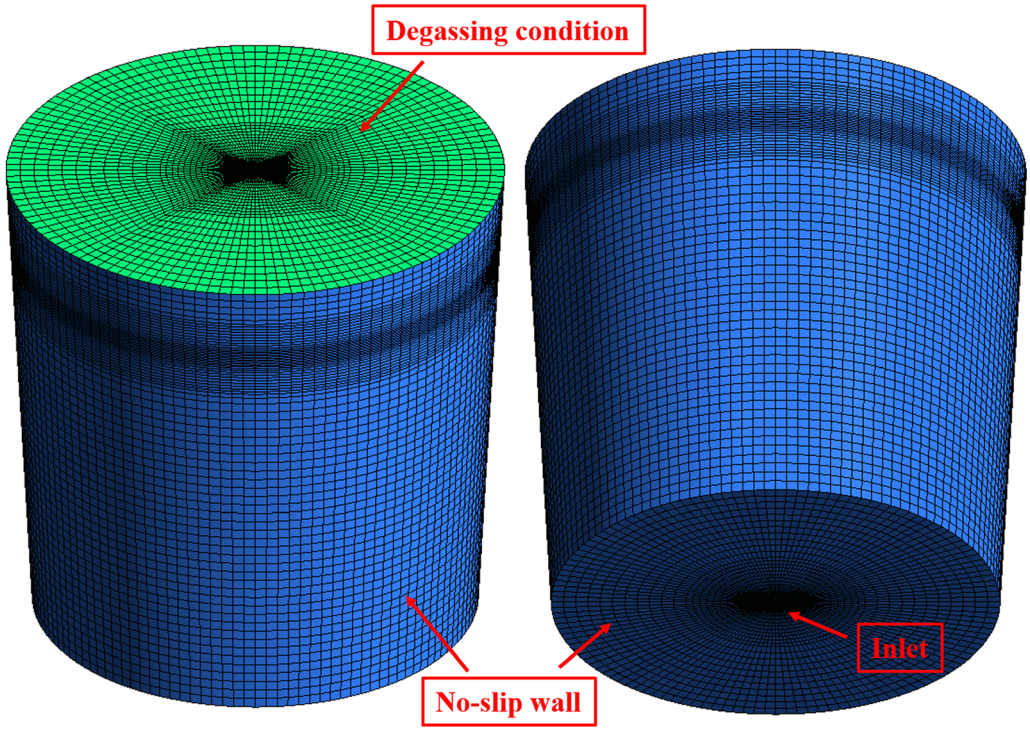

Fig. 2—Mesh quality and boundary conditions.

Table II. Five Different Models for the Drag Coefficient C_D

Model	Correlation	References
A	$C_D = \begin{cases} \frac{24}{Re} \cdot \left(1 + 0.15 \cdot \mathrm{Re}^{0.687}\right) & Re < 1000 \\ 0.44 & Re \geq 1000 \end{cases}$	Schiller and Naumann[19]
B	$C_D = \max\left[\min\left(C_{D,\mathrm{ellipse}}, C_{D,\mathrm{cap}}\right), C_{D,\mathrm{sphere}}\right]$ $C_{D,\mathrm{sphere}} = \max\left[\frac{24}{\mathrm{Re}} \cdot \left(1 + 0.15 \cdot \mathrm{Re}^{0.687}\right), 0.44\right]$ $\quad C_{D,\mathrm{ellipse}} = \frac{2}{3} Eo^{1/2}$, $C_{D,\mathrm{cap}} = \frac{8}{3}$	Ishii and Zuber[20]
C	$C_D = \max\left\{\min\left[\frac{24}{\mathrm{Re}} \cdot \left(1 + 0.15 \cdot \mathrm{Re}^{0.687}\right), \frac{72}{\mathrm{Re}}\right], \frac{8}{3} \cdot \frac{Eo}{(Eo+4)}\right\}$	Tomiyama *et al.*[21]
D	$C_D = \min\left[\max\left(C_{D,\mathrm{vis}}, C_{D,\mathrm{dis}}\right), C_{D,\mathrm{cap}}\right]$ $C_{D,\mathrm{dis}} = \frac{2}{3} \cdot \left[\frac{(g\rho_l)^{0.5} d_g}{\sigma^{0.5}}\right] \cdot \left[\frac{1+17.67\left(1-\alpha_g\right)^{1.286}}{18.67\left(1-\alpha_g\right)^{1.5}}\right]^2$ $\quad C_{D,\mathrm{vis}} = \frac{24}{\mathrm{Re}} \cdot \left(1 + 0.1 \cdot \mathrm{Re}^{0.75}\right)$, $C_{D,\mathrm{cap}} = \frac{2}{3}\left(1 - \alpha_g\right)^2$	Kolev[22]
E	$C_D = a_1 + \frac{a_2}{\mathrm{Re}} + \frac{a_3}{\mathrm{Re}^2}$ $\quad a_1$, a_2, and a_3 are constants that apply over several ranges of the Reynolds (Re) number of gas bubbles	Morsi and Alexander[23]

only has a significant effect on the plume near the inlet region because the deceleration process of the bubble is basically completed in this region. When the value of the coefficient increases to 0.5, the increased effect of the virtual mass force leads the bifurcation of the bubbly plume. This is why the gas volume fraction has a bimodal distribution when the virtual mass coefficient is 0.5. Compared with the measured values, the appropriate value of the virtual mass coefficient is in the range of 0.05 to 0.1 for the current model.

The effect of lift force on the bubbly plume structure is well known—that it just affects the distribution of gas bubbles in the radial direction. The optimal lift coefficients come from the different models having slight differences, but in general, they are in the range of 0 to 0.1. Lopez de Bertodano *et al.*[25] suggested a value between 0.02 and 0.1 in bubbly flows in the vertical duct. Sheng and Iron[26,27] determined a lift coefficient of 0.1 in unconfined plumes with small bubbles. Moreover, especially for the ladle simulation, Lou and Zhu[11] chose 0.01 as the optimal lift coefficient using the Eulerian–Eulerian approach, while Duan *et al.*[17] took a value of 0.1 using the Eulerian–Lagrangian approach. In this study, Figure 3(c) shows that the predicted values

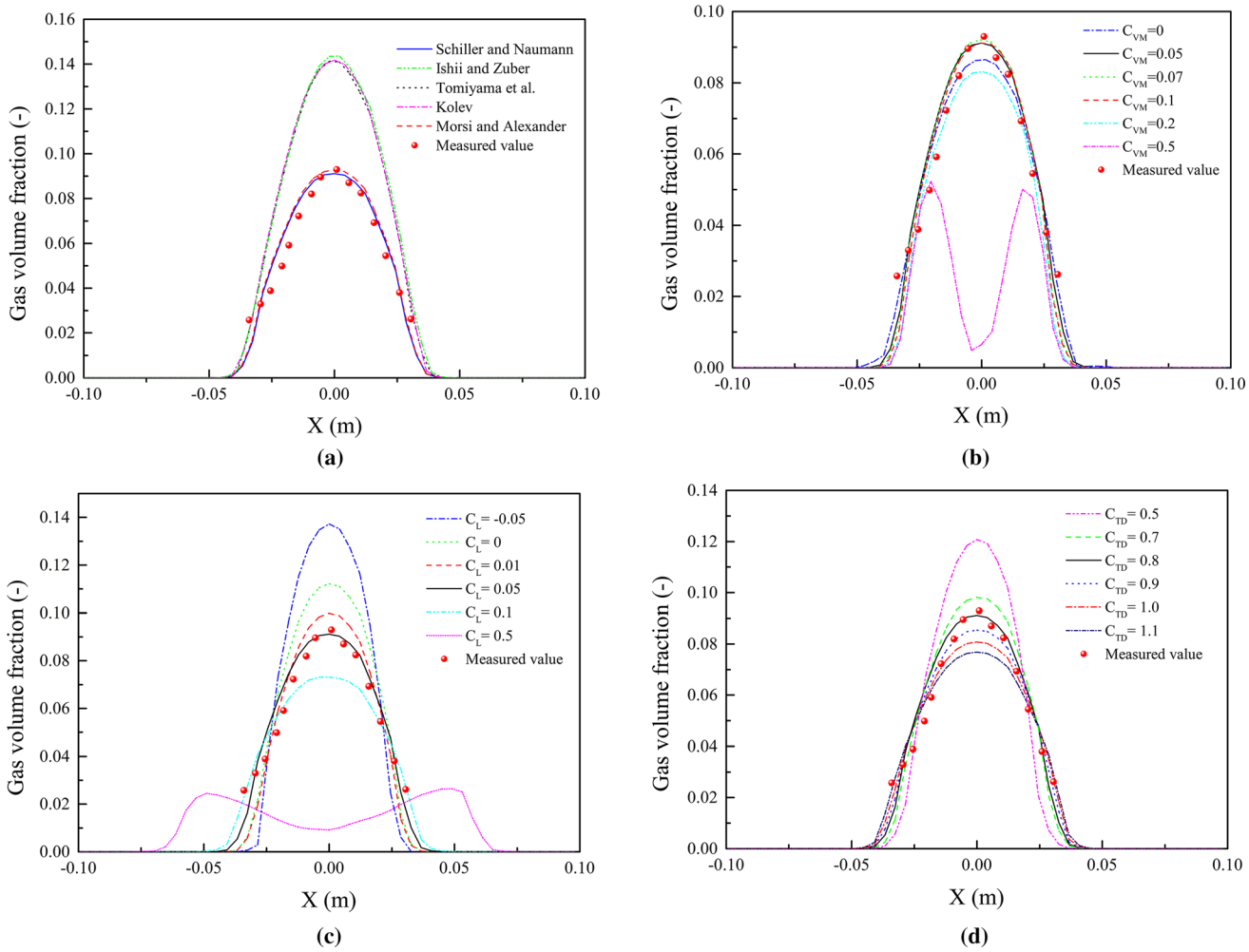

Fig. 3—Effects of the different interphase forces on bubbly plume structure at the height of 0.2 m; the gas flow rate is 12 L/min: (*a*) drag force, (*b*) virtual mass force, (*c*) lift force, and (*d*) turbulent dispersion force.

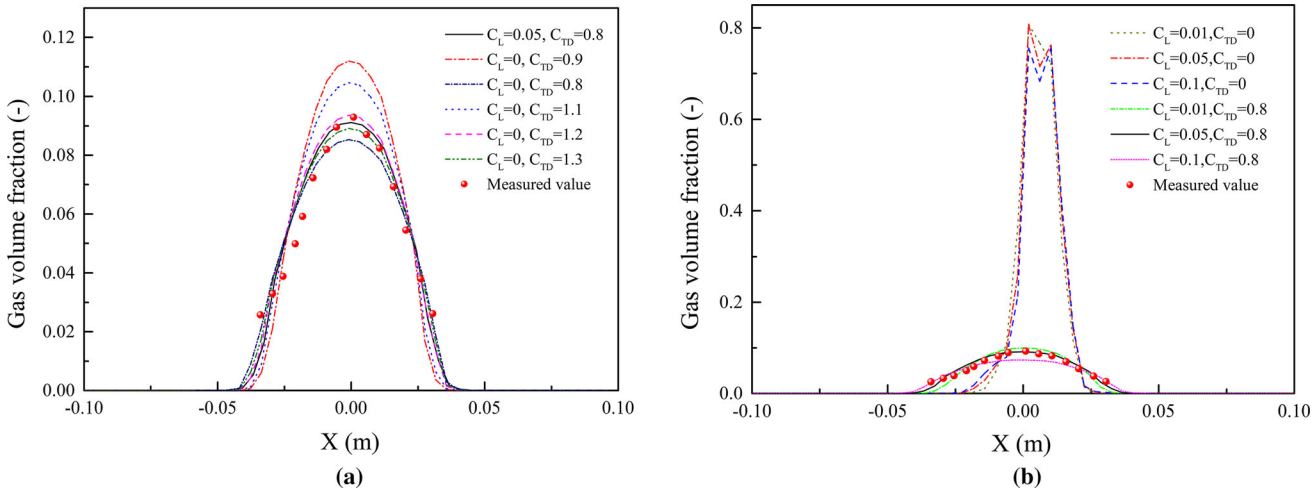

Fig. 4—Respective effects of the lift force and turbulent dispersion force on bubbly plume structure at the height of 0.2 m; the gas flow rate is 12 L/min: (*a*) turbulent dispersion force and (*b*) lift force.

have a better agreement with the measured values when the lift coefficient is set at 0.05. The smaller values of lift coefficient cause the narrower bubbly plume structures, whereas the structures become wider with the larger

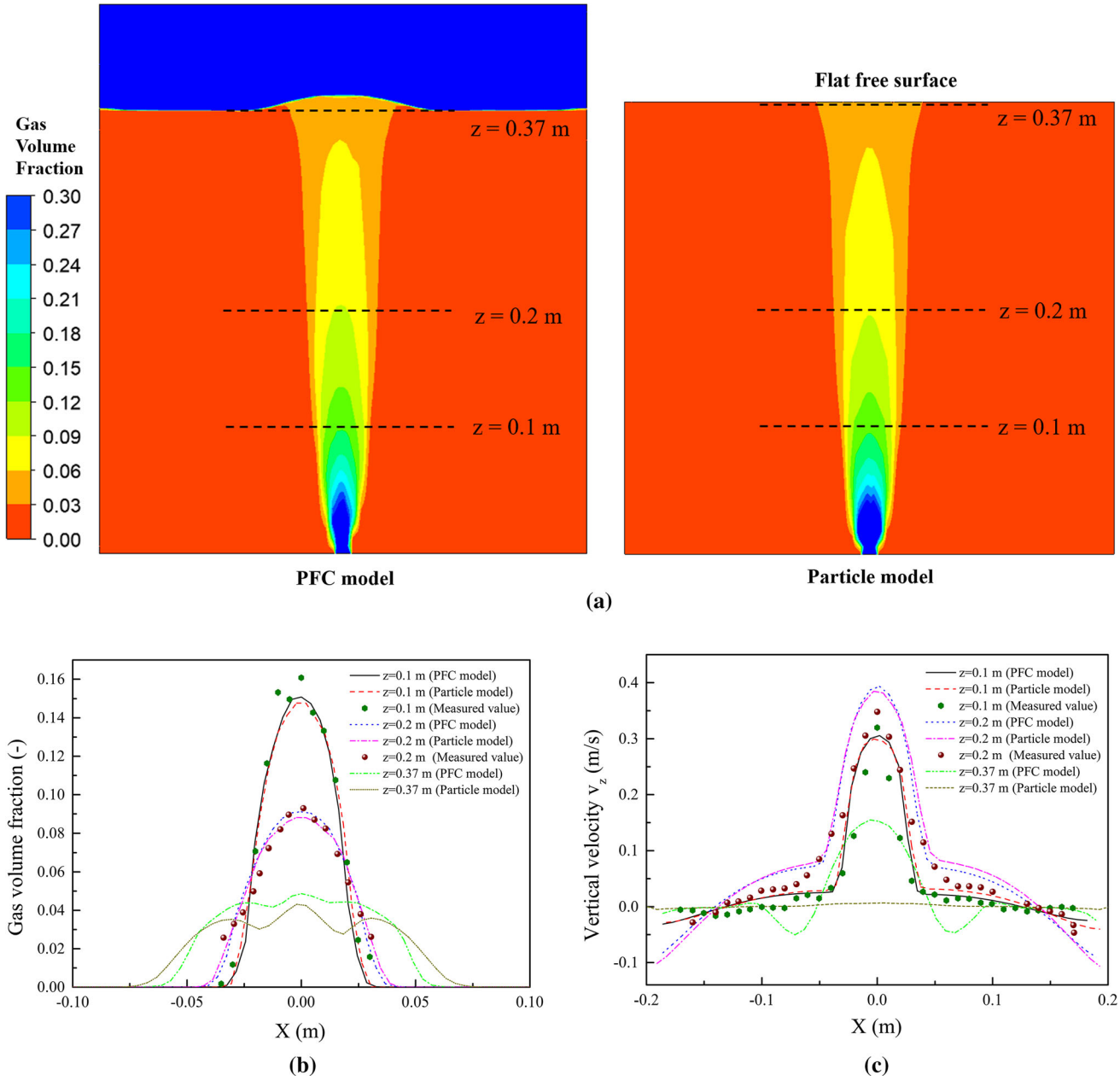

Fig. 5—Effects of the free surface setup on fluid flow, at the gas flow rate of 12 L/min: (*a*) predicted phase distribution, (*b*) gas volume fraction, and (*c*) liquid vertical velocity.

values. When the lift coefficient is 0.5, the horizontal spreading of the plume is very exaggerated and the gas volume fraction has a bimodal distribution. Figure 3(d) depicts the distribution of the bubble volume fraction with the different values of turbulent dispersion coefficient. The plume produces larger dispersion as a result of the higher turbulent dispersion coefficient. Compared to each turbulent dispersion coefficient, the predicted values correlate well with the measured values when a value of 0.8 is adopted.

It is not hard to find that both the lift force and turbulent dispersion force have influence on the radial distribution of gas bubbles. Therefore, it is very meaningful to consider alone their respective effects. Figure 4(a) shows that even though the model ignores the effect of lift force, the predicted values still can be close to the measured values by modifying the turbulent dispersion coefficient. Differently, when the turbulent dispersion force is not considered in the model, the predicted bubbly plume shape has a dramatic change, as shown in Figure 4(b). The width of the bubbly plume is extremely narrow and nearly keeps the same size along the vertical direction. Under this condition, there is no significant change as the values of the lift coefficient vary from 0 to 0.1. All the results prove that the influence weight of the turbulent dispersion force is higher than that of the lift force under the Eulerian–Eulerian

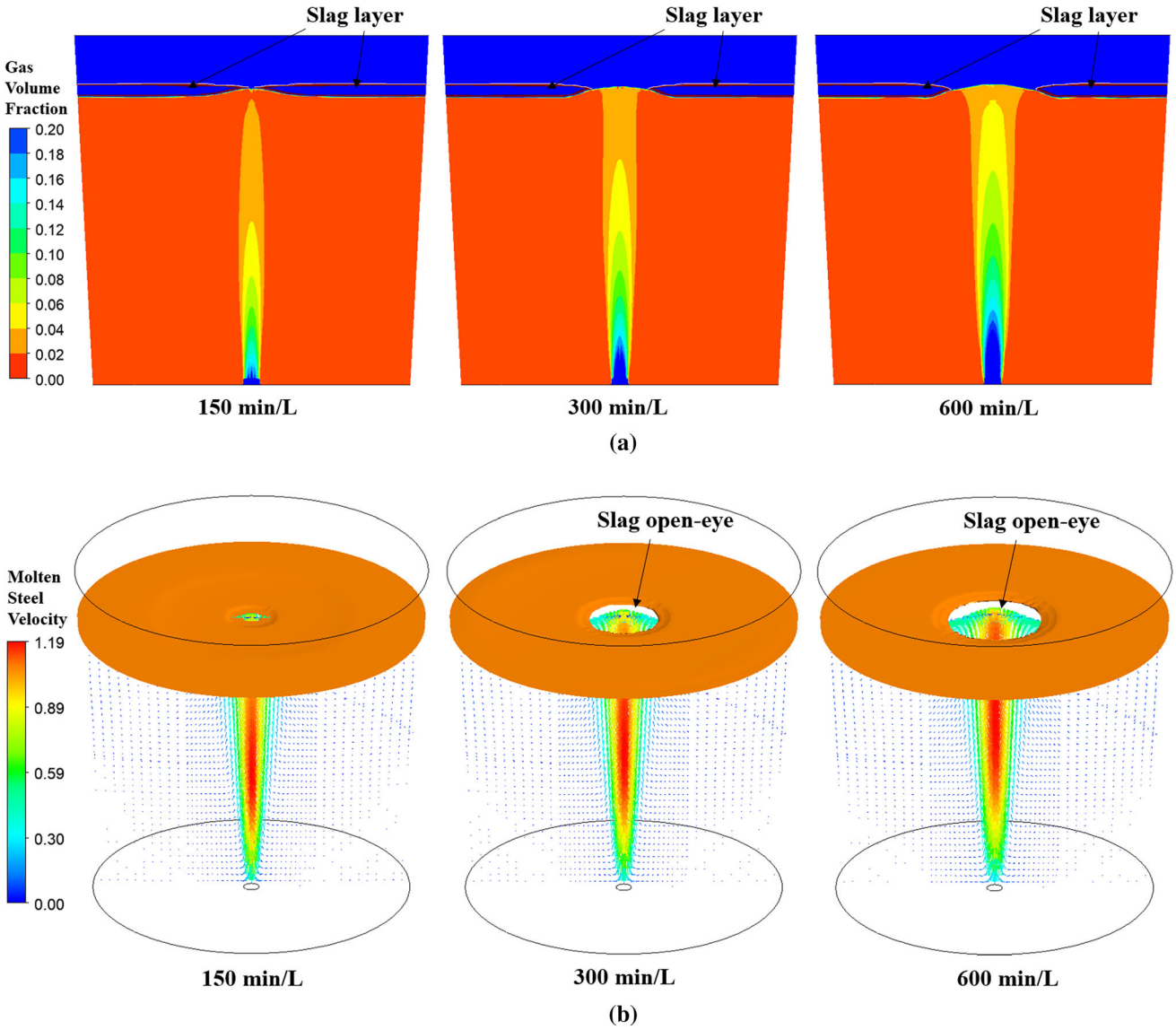

Fig. 6—Predicted results of industrial scale gas-stirred ladle under the different gas flow rates: (*a*) distribution of each phase at $Y = 0$ plane and (*b*) slag open-eye ($\alpha_s = 0.95$).

framework, and the model cannot neglect the turbulence dispersion force.

The effects of the free surface setup on fluid flow were investigated in this study. The simulation results predicted by the PFC model were chosen for comparison with the results predicted by the particle model in which the free surface was treated as flat. Figure 5(a) shows that the fluctuation of the liquid-free surface can be clearly presented in the PFC model, and there is a distinct bulge shape at the place where the gas bubbles flow out. Figure 5(b) depicts the gas volume fraction distribution at the different heights of the gas-stirred ladle, in conjunction with a comparison of measured values. As shown, the differences of the gas volume fraction distribution of the two models are not remarkable at $z = 0.1$ m and $z = 0.2$ m, and the predicted results correlate well with the measurements. Nevertheless, significant differences between the two models can be found at $z = 0.37$ m. Compared to the degassing condition boundary, it seems the fluctuation of the liquid-free surface has a function to prevent the gas bubble flowing out rapidly. Similar results can be seen in Figure 4(c)—that the differences of the liquid vertical velocity between the two models are negative at $z = 0.1$ m and $z = 0.2$ m. However, at $z = 0.37$ m, the liquid vertical velocity of the PFC model has different values along the liquid-free surface, while the liquid vertical velocity of the particle model is close to 0 m/s. All of the results indicate that the fluctuation of the liquid-free surface has an obvious influence on the floating behavior of gas bubbles near the region of the free surface. Therefore, in order to precisely predict the fluid flow in a gas-stirred ladle, it is requisite to consider the effect of the fluctuation of the liquid-free surface.

Since the present PFC model can reflect the fluctuation of the liquid-free surface, a recent hot topic, *i.e.*,

slag open-eye, also has been investigated in this study. An industrial scale gas-stirred ladle is modeled using the present PFC model, and the detailed model structure can be seen in Figure 1(b). All optimal coefficients have been employed, and other model parameters can be seen in Table I.

Figure 6(a) shows the distributions of the molten steel, gas bubble, and slag at the different gas flow rates. As seen, at the low gas flow rate (150 L/min), the bubbly plume is slim and the free surface of molten steel only has a slight fluctuation. As a result of the floating behavior of gas bubbles, the central slag layer is slightly broken and the slag open-eye starts to form. As the gas flow rate increases (300 and 600 L/min), the region of the bubbly plume gradually becomes wider and the central bulge becomes higher. The formation of slag open-eye is obvious. Figure 6(b) clearly shows that the higher the gas flow rate, the larger the slag open-eye. Unfortunately, because the numerical calculation is at a steady state, the phenomenon of slag entrainment does not emerge in this study.

To conclude, a PFC model was successfully developed and optimized for simulating the fluid flow in the gas-stirred ladles using the Eulerian–Eulerian approach. To accurately predict the fluid flow in a gas-stirred ladle, the fluctuating liquid-free surface must be considered in the model instead of using the flat and motionless boundary. Using the present model, various fluid flow phenomena, such as bubble trajectories, free surface fluctuations, and the formation of slag open-eye, can be simultaneously predicted for a wide range of gas flow rates during ladle stirring operations.

ABBREVIATIONS

A, A'	Interfacial area density and modified interfacial area density (–)
$\vec{F}$	Interphase force (N/m^3)
d_g	Initial diameter of gas bubble at the let (m)
$\vec{g}$	Gravity acceleration (m^2/s)
N	Number of bubble particles released from the inlet (–)
P	Pressure (Pa)
Q_g	Gas flow rate (m^3/s)
$\vec{v}$	Velocity (m/s)
V_{cell}	Grid cell volume (m^3)
$V_{bub,n}$	Volume of the nth bubble in the control cell volume (m^3)
α	Volume fraction (–)
ρ	Density (kg/m^3)
μ_l, $\mu_{l,t}$	Molecular viscosity and turbulent viscosity of the liquid phase (kg/(ms))

SUBSCRIPTS AND SUPERSCRIPTS

i, j	Phase or interacted phase
c, c'	Continuous phase
g	Gas phase
l	Liquid phase
s	Slag phase
t	Top gas phase
D	Drag force (N/m^3)
L	Lift force (N/m^3)
VM	Virtual mass force (N/m^3)
TD	Turbulent dispersion force (N/m^3)
ST	Surface tension force (N/m^3)

REFERENCES

1. Q. Cao, L. Nastac, A. Pitts-Gaggett, and Q. Yu: *Metall. Mater. Trans. B*, 2018, vol. 49B, pp. 988–1002.
2. S. Yu and S. Louhenkilpi: *Metall. Mater. Trans. B*, 2013, vol. 44B, pp. 459–68.
3. Y. Liu, M. Ersson, H. Liu, P.G. Jonsson, and Y. Gan: *Metall. Mater. Trans. B*, 2019, vol. 50B, pp. 555–77.
4. S.W.P. Cloete, J.J. Eksteen, and S.M. Bradshaw: *Progr. Comput. Fluid Dyn.*, 2009, vol. 9, pp. 345–56.
5. H. Liu, Z. Qi, and M. Xu: *Steel Res. Int.*, 2011, vol. 82, pp. 440–58.
6. L. Li and B. Li: *JOM*, 2016, vol. 68, pp. 2160–69.
7. L. Li, B. Li, and Z. Liu: *ISIJ Int.*, 2017, vol. 57, pp. 1980–89.
8. L. Li, W. Ding, F. Xue, C. Xu, and B. Li: *JOM*, 2018, vol. 70, pp. 2900–08.
9. *ANSYS Fluent User's Guide*, Release 17.0, Ansys Inc., Southpointe, 2016, pp. 1230–32.
10. Y. Sheng and G. Irons: *Metall. Mater. Trans. B*, 1993, vol. 24B, pp. 695–705.
11. W. Lou and M. Zhu: *Metall. Mater. Trans. B*, 2013, vol. 44B, pp. 1251–63.
12. A. Senguttuvan and G.A. Irons: *ISIJ Int.*, 2017, vol. 57, pp. 1962–70.
13. U. Singh, R. Anapagaddi, S. Mangal, K.A. Padmanabhan, and A.K. Singh: *Metall. Mater. Trans. B*, 2016, vol. 47B, pp. 1804–16.
14. E.K. Ramasetti, V.V. Visuri, P. Sulasalmi, R. Mattila, and T. Fabritius: *Steel Res. Int.*, 2019, vol. 90, p. 1900088.
15. Q. Cao and L. Nastac: *Metall. Mater. Trans. B*, 2018, vol. 49B, pp. 1388–1404.
16. L. Zhang and S. Taniguchi: *Int. Mater. Rev.*, 2000, vol. 45, pp. 59–82.
17. H. Duan, Y. Ren, and L. Zhang: *JOM*, 2018, vol. 70, pp. 2128–38.
18. Y. Xie, S. Orsten, and F. Oeters: *ISIJ Int.*, 1992, vol. 32, pp. 66–75.
19. L. Schiller and A. Naumann: *Vdi Zeitung*, 1935, vol. 77, p. 51.
20. M. Ishii and N. Zuber: *AIChE J.*, 1979, vol. 25, pp. 843–55.
21. A. Tomiyama, I. Kataoka, I. Zun, and T. Sakaguchi: *JSME Int. J. Ser. B*, 1998, vol. 41, pp. 472–79.
22. N.I. Kolev: *Multiphase Flow Dynamics 2: Thermal and Mechanical Interactions*, 3rd ed., Springer, Berlin, 2007.
23. S.A. Morsi and A.J. Alexander: *J. Fluid Mech.*, 1972, vol. 55, pp. 193–208.
24. D. Zhang, N.G. Deen, and J.A.M. Kuipers: *Chem. Eng. Sci.*, 2006, vol. 61, pp. 7593–7608.
25. M. Lopez de Bertodano, R.T. Lahey Jr, and O.C. Jones: *Int. J. Multiph. Flow*, 1994, vol. 20, pp. 805–18.
26. Y. Sheng and G. Irons: *Metall. Trans. B*, 1993, vol. 24B, pp. 695–705.
27. Y. Sheng and G. Irons: *Metall. Mater. Trans. B*, 1995, vol. 26B, pp. 625–35.